Microstructure and hydrothermal ageing of alumina-zirconia composites modified by laser engraving

Laurent Gremillard, L. Cardenas, H. Reveron, T. Douillard, A. Vogl, K. Hans, T. Oberbach

MICROSTRUCTURE AND HYDROTHERMAL AGEING OF ALUMINA-ZIRCONIA COMPOSITES MODIFIED BY LASER ENGRAVING

Published in Journal of the European Ceramic Society (2020), 40 pp. 2077-89
https://doi.org/10.1016/j.jeurceramsoc.2020.01.027

L. GREMILLARD[1,+], L. CARDENAS[2], H. REVERON[1], T. DOUILLARD[1], A. VOGL[1], K. HANS[3], T. OBERBACH[3]

[1] Univ Lyon, INSA-Lyon, CNRS, MATEIS UMR5510, F-69621 Villeurbanne, France
[2] Univ Lyon, CNRS, IRCELYON UMR5256, F-69100 Villeurbanne, France
[3] Mathys Orthopädie GmbH, Moersdorf, Germany
[+] Corresponding author: laurent.gremillard@insa-lyon.fr

ABSTRACT

Laser engraving is more and more commonly used to write permanent identity features on medical devices. In particular, it is performed on ceramic heads for hip prostheses. Since these components are submitted to high mechanical loading during long periods of time (several years), it is critical to assess the influence of laser engraving on their durability.
In the present article, laser marking of zirconia-toughened alumina and alumina-toughened zirconia resulted in an important colour change. It did not affect notably the resistance to hydrothermal ageing, despite important microstructural changes (in particular formation of a zirconia-alumina solid solution layer some tenths of micrometres thick). The formation of this original microstructure was explained by the fast cooling rate after lasing.

1. INTRODUCTION

Conforming with European regulations each medical device shall be identifiable and retraceable during production, storage, installation and servicing of product (ISO 13485:2016). Concerning medical implants, *e.g.* femoral heads for hip prosthesis, this regulation is realised by marking the components permanently with several numbers (among them the size and a serial number allowing its unique identification). The markings are also used by surgeons to verify the chosen head size during surgical intervention. Several techniques are implemented to make this type of permanent marks; among them, the most commonly used is laser engraving (LE). Laser engraving involves a number of modifications (morphological changes, chemical and structural evolutions…) localised on and below the surface that may impact the durability of the marked devices. The present work is focused on laser engraving – induced modifications on zirconia-alumina composites used for hip-joints heads.
Laser treatments of zirconia-based bioceramic materials have also attracted extensive attention thanks to their ability to tailor and tune interfacial properties. For instance, the surface features induced by laser may be interesting for improved biointegration [1–3], by influencing the adhesion of osteoblasts. Lasing is also used to improve the zirconia-porcelain bonding strength [4,5] or to change the lased surface hydrophilicity[6].

Laser engraving of oxide ceramics generates both morphological changes and a darkening of the lased areas. The morphological changes can be explained quite easily in terms of melting / ablation phenomena [7]. However, several hypotheses exist to explain the apparition of the

colour: formation of ZrN [6,8] or ZrC [9], of colour centres [10], or of oxygen vacancies [11]. To our knowledge none of them is completely proven in the case of zirconia-based composites.

As far as zirconia-based ceramics are concerned, two properties controlling the reliability of the orthopaedic devices may be significantly impacted by lasing: resistance to crack propagation (if the laser marking leads to the creation of large defects) and resistance to hydrothermal ageing [12] (the marked area may become more prone to tetragonal-to-monoclinic (t-m) transformation in the presence of water). Indeed the lased ceramic areas are often microcracked [13,14], which may offer a path for water to diffuse in the subsurface of the material and accelerate ageing. Moreover, lasing a material is equivalent to a fast thermal treatment, with high deposited energy and very high heating and cooling rates. This may give rise to peculiar microstructures and residual mechanical stresses that are known to influence ageing kinetics [14,15]. Indeed an acceleration of the ageing kinetics of zirconia was observed after lasing[16], explained by the formation of monoclinic phase and of residual stresses during lasing. The surface and sub-surface modifications also affect the mechanical properties. This was studied in particular by Roitero et al. [17] who observed a decrease in strength (but an increase of Weibull modulus) after lasing zirconia samples with a nanosecond Nd:YAG laser.

The literature on laser treatment of zirconia-alumina based composites is rather scarce. Femtosecond laser was used to machine dental ceramic implants made of zirconia-toughened alumina (ZTA) [18], or to induce regular patterns on an alumina-toughened zirconia (ATZ) surface [19]. And similarly to what was attempted in monolithic zirconia, laser-modifications of alumina-zirconia composites were used to induce osteogenic differentiation of human mesenchymal stem cells [20] and favour viability of osteoblast-like cells [21], or to help osseointegration of endosseous dental implants [22].
In addition to the microstructural changes induced in zirconia by the melting/ablation/quenching sequence, alumina-zirconia composites show also chemical changes, as reported by Ackerl et al. [18] who reported that “Alumina […] seemed to dissolve approaching the surface”.

In the present work, the influence of laser marking of zirconia-toughened alumina (ZTA) and alumina-toughened zirconia (ATZ) on hydrothermal ageing kinetics, microstructure and colour changes was studied. Remarkable microstructural changes were evidenced. However, they did not seem to affect the resistance of the materials to hydrothermal ageing.

2. MATERIALS AND METHODS

2.1 MATERIALS

Disk-shaped samples (20 mm diameter) were hot isostatically pressed (HIP) and laser-engraved by Mathys Orthopädie GmbH (Mörsdorf, Germany). All of them were then sterilized by gamma radiation issued from a Co-60 source with a radiation dose between 25 – 45 kGy. Two different materials were tested: alumina-toughened zirconia (ATZ, ceramys®, composed of 80 wt.% 3 Y-TZP and 20 wt.% α-Al_2O_3, i.e. 72.4 and 27.6 vol.% respectively) and zirconia-toughened alumina (ZTA, symarec®, composed of 75 wt.% α-Al_2O_3 and 25 wt.% 3 Y-TZP – i.e. 82.0 and 18.0 vol.% respectively).
A 10×8 mm² zone was laser engraved in each disk, following a path consisting of parallel lines, the engraving path being a series of parallel lines separated by 50 µm (hatch distance) and with

0.4 µs pulse duration. Three conditions were applied for each material (hereinafter referred to as lot1, 2 and 3), as shown on Table 1. The samples of lot 1 have been laser engraved as green bodies (meaning that these sampled were sintered after lasing) with a Nd:YAG laser, adjusting the laser conditions depending on the material: ATZ was engraved with a higher laser power, pulse frequency but lower scanning speed than ZTA. The samples of lot 2 and lot 3 have been laser engraved as sintered bodies with a Nd:YVO_4 laser. For both lots and both materials the same laser parameters have been used, except the scanning speed. Lot 2 has been produced under standard laser conditions. For both lots 1 and 2, the laser parameters were selected based on a balance between marking time, visibility and homogeneity of the colour after marking. For lot 3 the deposited energy is 8 and 4 times higher than for lot 2, respectively for ATZ and ZTA, due to 8 or 4 times lower scanning speeds (resp. for ATZ and ZTA, all other parameters being kept constant). Lot 3 is thus considered as a "worst case", expected to exaggerate the microstructural features obtained with lot 2.
In the following, the samples will be referred to as "Material-XXn" with material being ATZ or ZTA, XX referring to the material state (LE: Laser Engraved zone; AR: pristine, As Received material) and n to the lot number (1, 2 or 3) (for example, ATZ-LE3 refers to the laser-engraved zone of ATZ ceramic engraved with the most severe conditions (lot 3)).

Table 1 : Samples (in all cases pulse duration is 0.4 µs, and engraving is performed in air)

Material	**ATZ**			**ZTA**		
Lot	1	2	3	1	2	3
Laser engraved as	Green body	Sintered body		Green body	Sintered body	
Laser type, wavelength	Nd:YAG, 1064 nm	Nd:YVO_4, 532 nm		Nd:YAG, 1064 nm	Nd:YVO_4, 532 nm	
Power (W)	2.56	7.00		1.88	7.00	
Pulse Frequency (Hz)	7000	18000		3000	18000	
Speed (mm/s)	60	400	50	80	100	25
Example					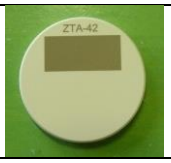	

2.2 EXPERIMENTAL METHODS

2.2.1 Accelerated Ageing Tests

To simulate the hydrothermal ageing of zirconia, the samples were placed in an autoclave (Sanoclav LA-MCS, Wolf, Germany), in contact with water vapour at various set temperatures (111, 134 or 141°C, 3 samples for each temperature) during different exposure times up to 450h.

At different time points during the ageing test, the fraction of monoclinic zirconia in the samples was measured by X-Ray Diffraction (XRD), distinguishing between AR and LE zones.
At a given temperature, the degree of advancement of the tetragonal-to-monoclinic transformation (f_m) as a function of ageing time (t) curve was fitted using the Mehl-Avrami-Johnson law (MAJ):

$$f = \frac{V(t)-V_0}{V_M-V_0} = 1 - \exp(-(bt)^n) \qquad \text{(Eq. 1)}$$

where *V(t)* is the volume fraction of monoclinic zirconia at time *t* (determined by XRS, as shown later in section 2.2.2), V_0 the monoclinic volume fraction before ageing, V_M the saturation monoclinic volume fraction (after the whole ageing process), *n* a constant between 0,5 and 4, *b* a parameter depending on the microstructural features and the temperature. For temperatures between ~25 and ~150°C, the ageing process is thermally activated so that parameter *b* follows an Arrhenius' equation, as follows:

$$b = b_0 \exp(-\frac{Q}{RT}) \qquad \text{(Eq. 2)}$$

where b_0 is a constant, *Q* the activation energy of the process (J/mol), *R* the gas constant (J/mol/K) and *T* the absolute temperature (K).
All the variables V_0, V_M, *n*, b_0 and *Q*, that are characteristic of the materials and may vary also with residual stresses, surface treatments…, were determined using the procedure described by Gremillard et al. [23].

Knowing the activation energy Q, the ageing process at high temperatures (indicated by subscript 1 in eq. 3) is correlated with that at 37°C (*in vivo* temperature, indicated by subscript 2): the same monoclinic fraction is reached for both (T_1, t_1) and (T_2, t_2) conditions, as follows:

$$t_2 = t_1 \cdot \exp(-\left(\frac{Q}{R}\right) \cdot \left(\frac{1}{T_1} - \frac{1}{T_2}\right)) \qquad \text{(Eq. 3)}$$

Using this equation the evolution of zirconia ageing with time at any temperature between room temperature and ~150°C was predicted.

2.2.2 Physico-chemical and morphological characterisation

X-Ray Diffraction was used to identify the crystalline phases and to determine the amount of monoclinic phase in the LE-zone and in the AR-zone of the ceramic discs, using a D8-ADVANCE diffractometer (Bruker) with a CuK_α radiation. . The XRD patterns where also analysed by using Rietveld refinement based on the TOPAS® software. Here the scan range was from 20 to 80° of 2θ, with step size of 0.01° and measuring time of 2s/step.

The volume fraction of monoclinic zirconia (*V(t)*) was calculated from the diffractograms obtained on ATZ and ZTA materials (before and after ageing) using Garvie and Nicholson's equation modified by Toraya [24,25]:

$$V(t) = \frac{1{,}311 \cdot X_m}{1 + 0{,}311 \cdot X_m}, \text{ with } X_m = \frac{I_m^{(-111)} + I_m^{(111)}}{I_m^{(-111)} + I_t^{(101)} + I_m^{(111)}} \qquad \text{(Eq. 4)}$$

where $I_x^{(hkl)}$ represents the area under the peak created by the crystallographic plane *(hkl)* of the phase *x* (*m* stands for the monoclinic phase and *t* for the tetragonal phase).

However, as this method only enables to measure a weighted average amount of monoclinic zirconia over the first micrometres below the surface of the sample (~5 µm for ATZ and ~15 µm for ZTA), cross-sections of selected materials were also characterized by Scanning Electron Microscopy associated with Energy Dispersive X-ray Spectroscopy (SEM-EDS, Zeiss SUPRA VP55 equipped with and Oxford SDD EDS detector). These cross sections were prepared by cross-sectioning with a diamond blade followed by planar argon ion milling (Illion, Gatan, USA). Using argon ion milling prevents the apparition of monoclinic phase associated to more classical mechanical polishing procedures. Most SEM images were obtained using a 2 kV acceleration voltage, while EDS spectra were recorded using 5 or 15 kV acceleration voltage in partial vacuum conditions (chamber pressure around 20 Pa of gaseous nitrogen).
Besides, cross-section observations and 3D serial sections (allowing the reconstruction of the observed volume) were also performed by Focused Ion Beam (FIB-SEM, NVision 40 (Carl Zeiss Microscopy GmbH, Oberkochen, Germany) combining a SIINT zeta FIB column (Seiko Instruments Inc. NanoTechnology, Japan) with a Gemini I column.

Special care was taken during all FIB experiments to minimise curtain effect and surface implantation, and to avoid any ion beam induced tetragonal-to-monoclinic transformation of the zirconia phase. Prior to serial sectioning, a sufficient cross-sectional area was freed to minimise as much as possible the shading effects. To perform this step, coarse ion beam currents ranging from 13 nA to 3 nA at 30 keV were used. Then, careful milling at 30keV/700pA was applied for serial sectioning. Image / volume reconstructions and analyses were performed using the FIJI software.

Topography and chemical compositions were also assessed by SEM-EDS. Moreover, optical 3D Microscope (KH-7700 Digital Microscope System, HIROX Europe Ltd.) was used to study the waviness and roughness of the LE-zones, mainly by measuring the height and spacing of the ridges (peak-to-valley depth and peak-to-peak distance) created by the laser engraving process.

3. RESULTS

3.1 AGEING BEHAVIOUR

3.1.1 Alumina-toughened zirconia (ATZ)

The ageing kinetics of alumina-toughened zirconia are shown on Figure 1. At high temperature (between 111 and 141 °C) they show no significant influence of laser treatments 1 and 2 as compared to the non-treated zones. However laser treatment 3 seems to slightly delay ageing, at least at temperatures above 100°C. The parameters of the ageing process are reported in Table 2. This table shows that the activation energies for ATZ-LE2 and ATZ-LE3 are significantly smaller than the ones for ATZ-LE1 and ATZ-AR, which explains why, while performing better against ageing at high temperature, ATZ-LE2 and ATZ-LE3 age faster at *in vivo* temperature (37°C / body temperature), as can be seen on Figure 1-b.
Also it can be noticed that AR and LE1 areas exhibit perfectly similar behaviours, either at high temperature or after extrapolation at body temperature. This is an indication that sintering erased all physico-chemical modifications brought by laser treatment, including the dark colour.

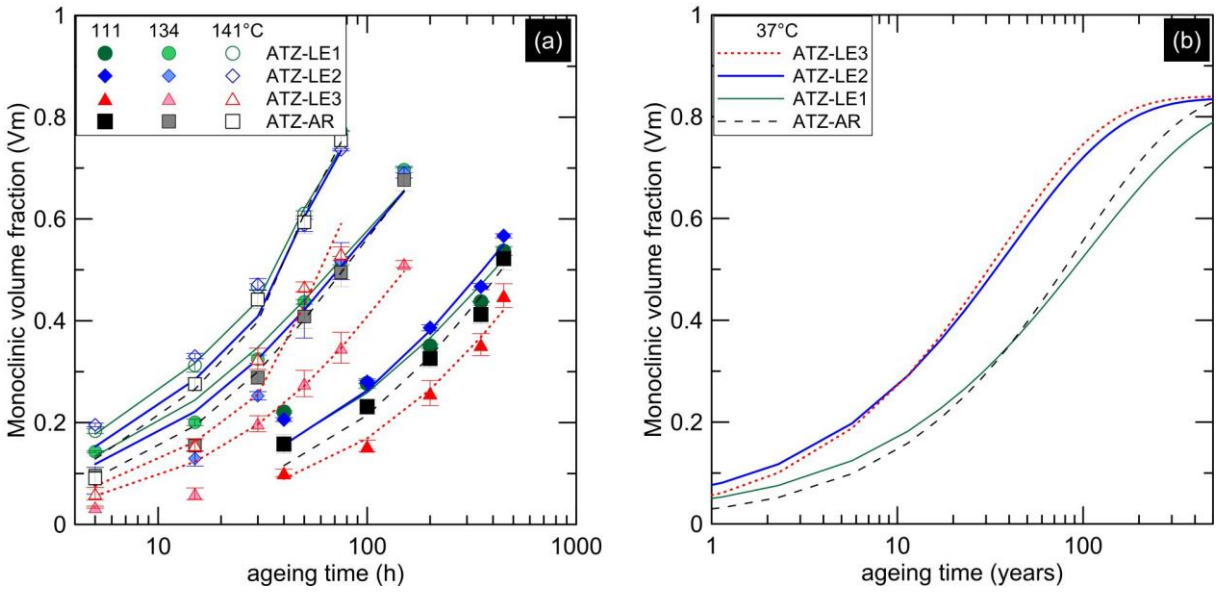

Figure 1: ageing kinetics of ATZ: (a) measured at 111, 134 and 141°C and (b) extrapolated at 37°C.

Table 2: ageing parameters of ATZ.

	ATZ-AR	ATZ-LE1	ATZ-LE2	ATZ-LE3
Q	98.4	101.0	89.8	80.9
n	0.759	0.660	0.726	0.752
b_0	$4.74 \cdot 10^{10}$	$1.16 \cdot 10^{11}$	$4.00 \cdot 10^{9}$	$1.40 \cdot 10^{8}$
V_0	0.002	0.012	0.022	0
V_M	0.852	0.840	0.836	0.84

3.1.2 Zirconia-toughened alumina (ZTA)

The ageing kinetics of zirconia -toughened alumina are shown on Figure 2. Again they show no significant influence of laser treatment 1 as compared to the non-treated zones (all the data of lot 1 and AR were thus considered together to calculate the ageing parameters of non-treated areas). However ageing speed seems to increase with the severity of the laser treatment, since LE3 areas age faster than the LE2 ones, themselves being more sensitive than the non-treated ones. The parameters of the ageing process are reported in Table 3. Even if this table shows activation energies much smaller for AR surfaces and lot 1 than for ZTA-LE2 and ZTA-LE3, at body temperature the same hierarchy as at high temperature is found.
In any case, hydrothermal ageing of ZTA is very limited, the calculated monoclinic fraction reaching at most 5% of the total zirconia content after 100 years at body temperature.

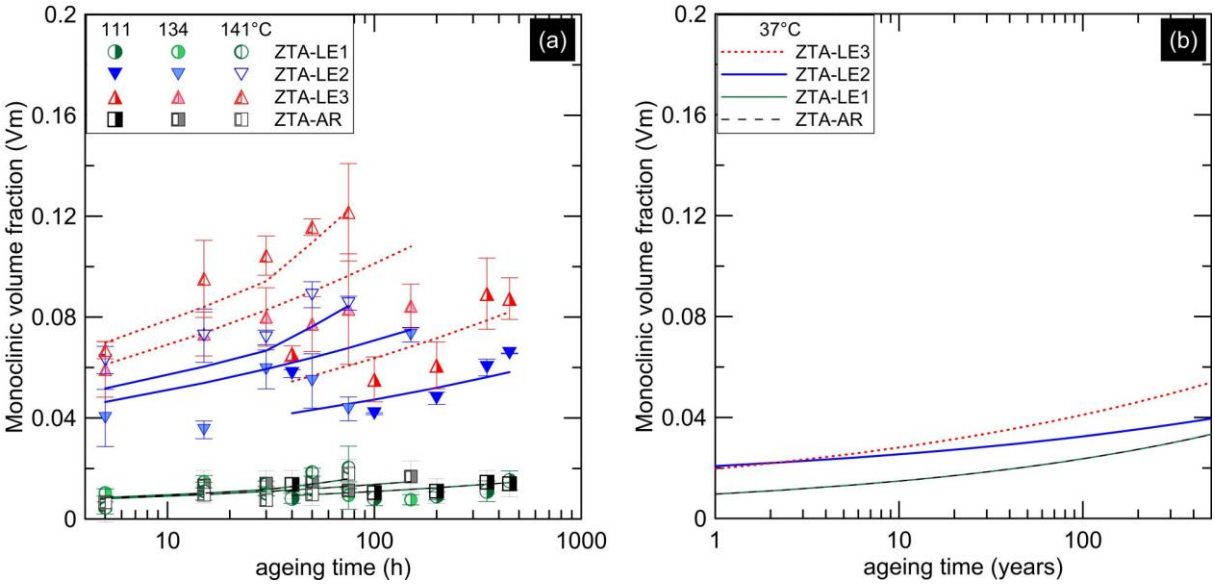

Figure 2: ageing kinetics of ZTA: (a) measured at 111, 134 and 141°C and (b) extrapolated at 37°C.

Table 3: ageing parameters of ZTA

	ZTA-AR	ZTA-LE1	ZTA-LE2	ZTA-LE3
Q	68.8	68.8	161.0	155.9
n	0.242	0.242	0.187	0.201
b_0	1.00	1.00	$5.57 \cdot 10^{13}$	$2.67 \cdot 10^{15}$
V_0	0.003	0.003	0.012	0.005
V_M	0.502	0.502	0.532	0.375

3.2 MACROSCOPIC SURFACE MORPHOLOGY

The depth engraved by the laser strongly depends on the material (ATE or ZTA) and on the engraving conditions (lot 1, 2 or 3). Figure 3 (a-b) shows examples of height profiles of the LE-zone. In both materials, the profiles of LE1 are the most irregular, and the profiles of LE3 are the sharpest; lot 2 present intermediate features, with slightly smaller engraving depth than lot 1 in average but more regular shape. Note that due to shrinkage during sintering the peak-to-peak distance (when measurable) is smaller in lot 1 (Table 4).

In both LE2 and LE3, a black colour makes the engraving visible to the naked eye, while the engraving depth is high enough to allow a clear detection of periodic ripples by 3D microscopy (Figure 3-c). However, on ATZ-LE1 and ZTA-LE1 the engraving is sometimes barely visible by the 3D microscope (Figure 3-d), with engraving depth around 1 µm.

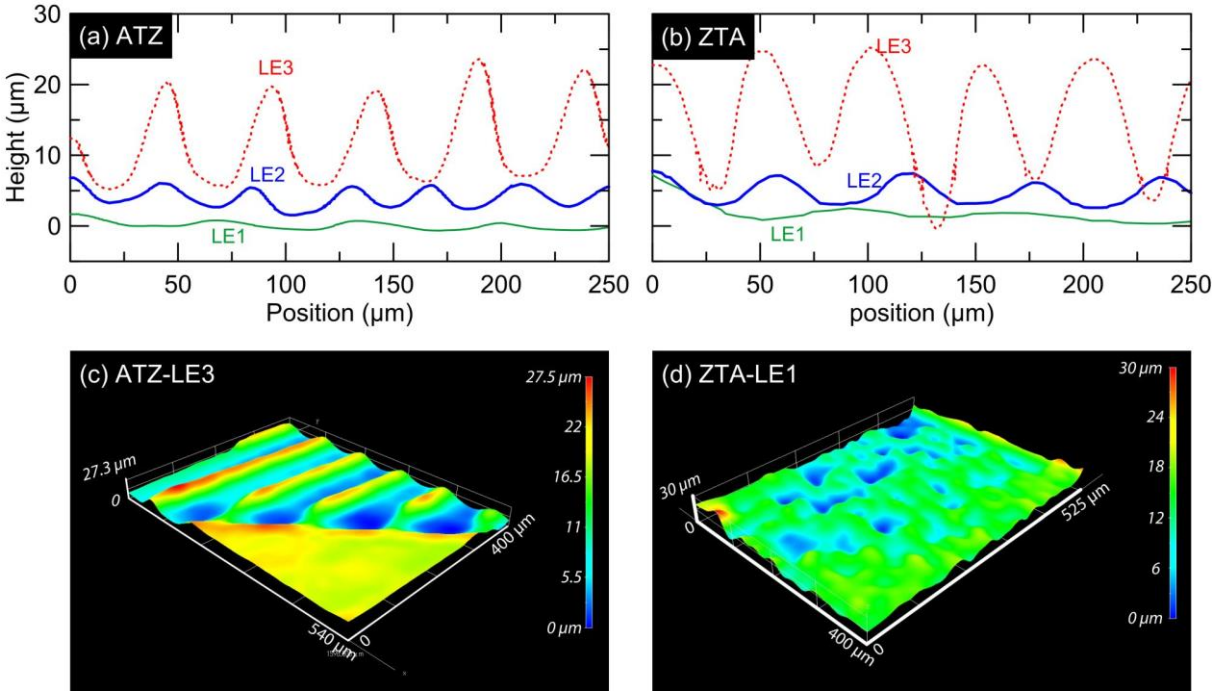

Figure 3: Profiles of the laser engraved zone for (a) ATE and (b) ZTA with the different engraving conditions; 3D-microscope micrographs of the frontier between AR and LE zones for (c) ATZ lot 3 and (d) ZTA lot 1.

Table 4: Average and standard deviation of measurements of the ridge's height and the laser pitch for samples of every material and lot.

Sample	Peak-to-valley depth (µm)	Peak-to-peak Distance (µm)
ATZ-LE1	3±1	44±5
ATZ-LE2	2±1	49±5
ATZ-LE3	16±3	51±4
ZTA-LE1	7±3	Not measurable
ZTA-LE2	5±1	48±3
ZTA-LE3	17±1	51±3

3.3 MICROSTRUCTURAL ANALYSIS

3.3.1 Microstructure of ATZ

Surface microstructural features of ATZ and ZTA samples (AR and LE) are shown in Figure 4. Top views of ATZ-AR materials reveal only the machining patterns and the classical microstructure of ATZ composites after sintering (alumina and zirconia grains). On LE areas, all patterns engraved by the laser are clearly seen. However, they are much more visible in ATZ-LE3 than in ATZ-LE1 and ATZ-LE2.
ATZ-LE1 exhibits also the classical microstructure of ATZ material, with clearly defined zirconia and alumina grains, although the surface is very rough.
ATZ-LE2 and ATZ-LE3 show some "cauliflower" structures on their surface (Figure 4-h), believed to have been recrystallized from the material evaporated by the laser since they mainly appear on the bottom of the laser tracks. Cracks can also be detected running all along the lased zones, especially in ATZ-LE3 (Figure 4-g).

Cross-sectional view of ATZ-LE2 reveals the existence of two thin layers of material on top of the bulk material (Figure 5 (a-b)). The first one (light grey - coloured and dense), attached to the bulk, appears to be made of a zirconia-alumina solid solution (see EDX maps, Figure 5 -(c-f)). Although this layer is too thin to be very precisely analysed, EDX analysis shows it contains an approximate proportion of ~25 wt.% alumina, close to the average alumina fraction in the ATZ material (20 wt.%). The second, uppermost one (dark-grey-coloured and porous) is enriched with carbon (which may be due either to contamination during the engraving, the laser engraving having been performed in air, or to sample preparation artefacts). Figure 5 also shows the presence of short cracks initiated on the surface of LE2, apparently running less than 1 µm deep.

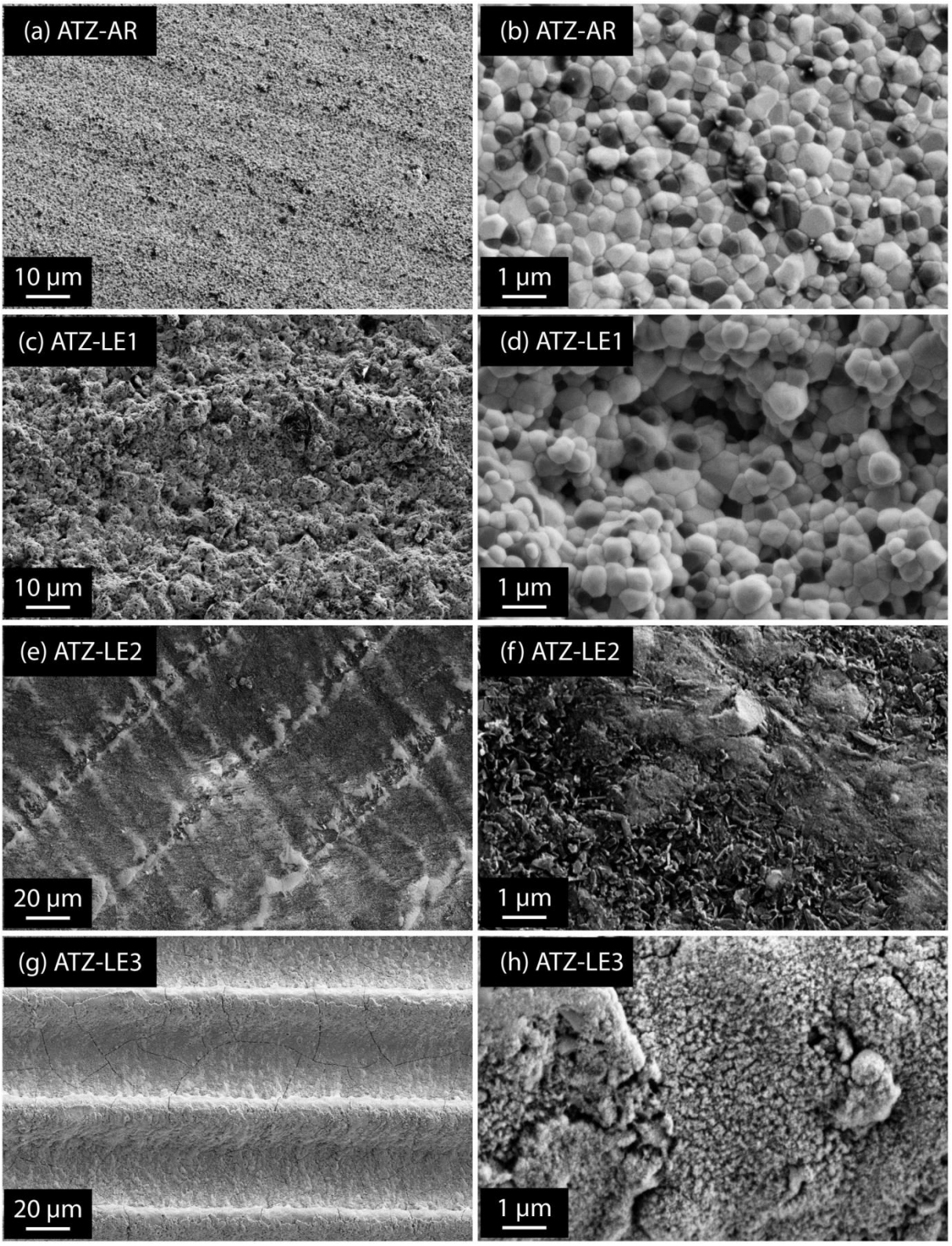

Figure 4: top view by SEM of ATZ material on as received (AR) and laser engraved (LE) zones

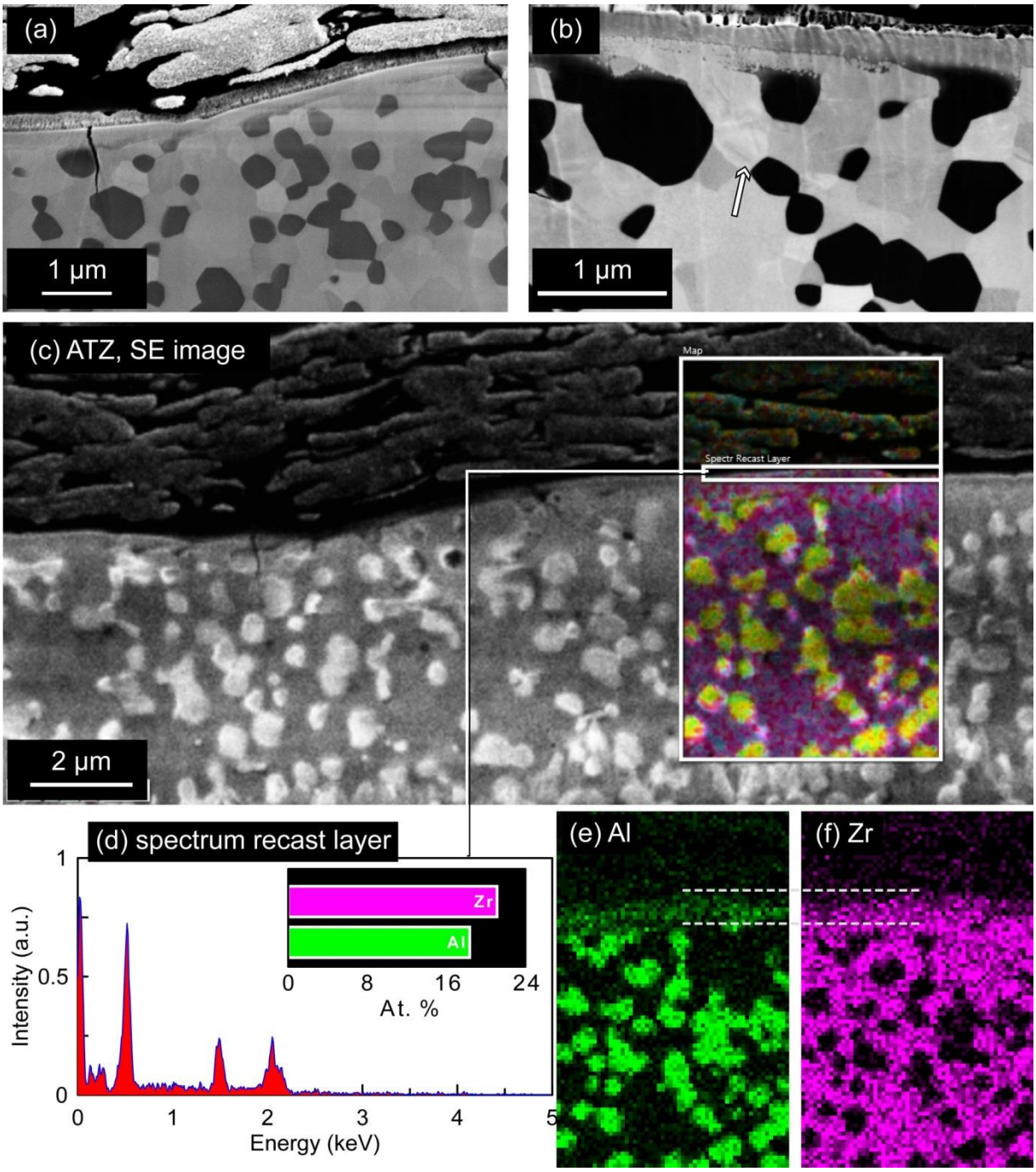

Figure 5: Cross-sectional views of ATZ-LE2. (a) and (b): SEM (zirconia appears in white, alumina in black, due to atomic number contrast born by back-scattered electrons). The arrow in (b) points to a grain containing monoclinic laths. (c)-(f): EDS analysis: (c) SE superposition, (d) spectrum of the recast layer, (e) Al map, (f) Zr map. In (c) here zirconia appears in black and alumina in white, due to a conductivity contrast). The dashed white lines in (e) and (f) indicate the location of the alumina-zirconia solid-solution layer.

The 3D-FIB reconstruction performed on a cross section of ATZ-LE2 just below the surface confirms the presence of the two layers observed on SEM cross sections (Figure 6). Nevertheless, it remains difficult to precisely characterize the exact composition of these two layers. Indeed, their thickness is lower than 500 nm, while the spatial resolution of EDS in SEM is of the same order of magnitude. Thus the EDS signal detected from this layer contains also signal from the surrounding material. Figure 6-c represents a cross section of the volume shown

in (a), and (d) to (h) are top views at different depth (orthogonal to (c) (thus parallel to the surface) calculated from the 3D-reconstruction of Figure 6-a. These figures show the evolution of the microstructure with depth. The first layer (<150 nm deep, Figure 6-d) shows this "cauliflower" structure observed by SEM on the surfaces of LE2 (and LE3). 300 nm under the surface (Figure 6-e) a layer of homogeneous composition (the zirconia-alumina solid solution) is found. 700, 800 and 900 nm under the surface (Figure 6-(f-h)) the material becomes biphasic, with large interphases between alumina grains and zirconia matrix, as if the alumina grains were partially molten. The microstructure of the as-prepared ATZ material, with well-defined alumina and zirconia grains, can only be found 1 µm under the surface and below (Figure 6-ei. Figure 6-b also shows the presence of a seemingly large crack. In fact this crack may be relatively long, but it is mainly a surface crack and does not go very deep inside the material (2.5 µm at most).

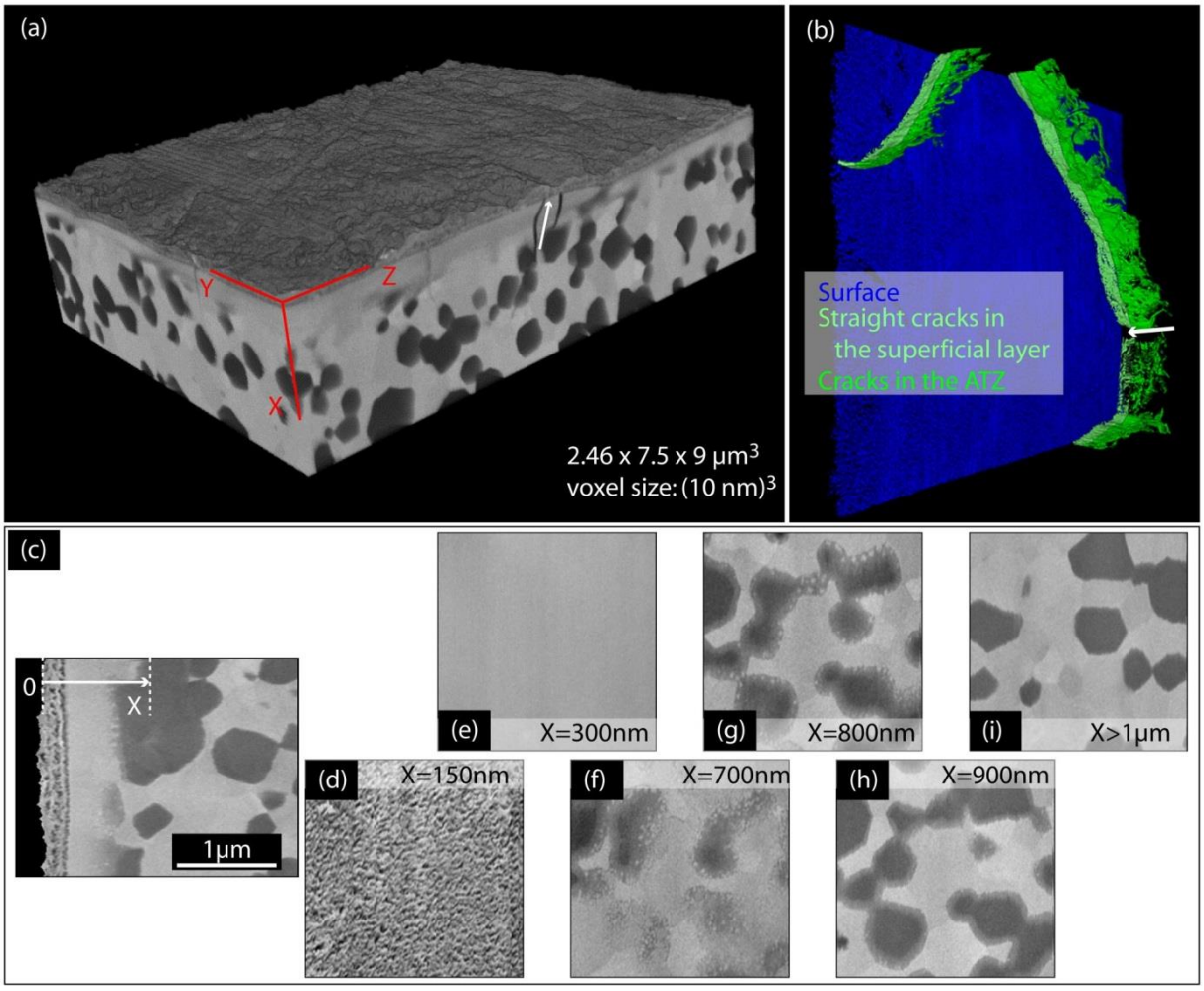

Figure 6: (a) 3D FIB reconstruction of the sub-surface of ATZ-LE2; (b) crack network extracted from (a) (the arrows in (a) and (b) point to the same location); (c): cross section extracted from (a). (d)-(h) sections parallel to the surface (orthogonal to (c)), showing the evolution of the different phases with depth in ATZ-LE2; the sections cover the depth indicated by the 2 dashed lines in (c). Zirconia grains appear in white, alumina in grey.

On ATZ-LE1 zones the alumina-zirconia solid solution layer is found neither before nor after hydrothermal ageing (Figure 7). However the carbon layer is sometimes apparent (not shown), which confirms that it possibly comes from some sample preparation artefacts (since the carbon should have disappeared during sintering).

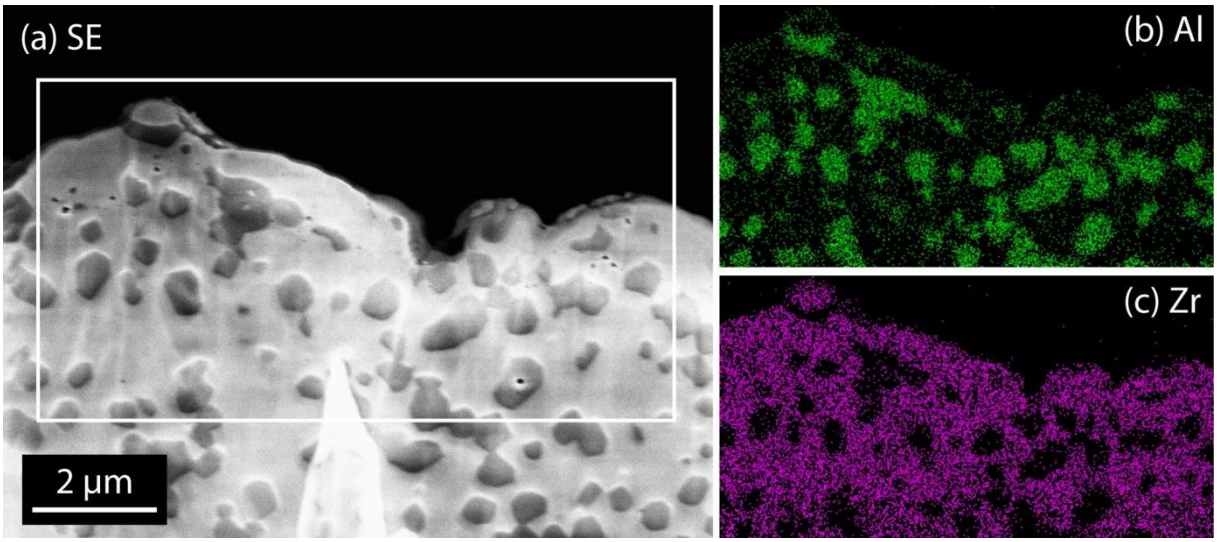

Figure 7: EDS map of the cross-section of ATZ-LE1; (a) Secondary electrons image (alumina in black, zirconia in white); (b) Aluminium map; (c) Zirconium map.

3.3.2 Microstructure of ZTA

Top views (Figure 8) of ZTA-AR materials reveal only the machining patterns and the classical microstructure of ZTA after sintering, with clearly distinguishable alumina and zirconia grains. On LE zones, all patterns engraved by the laser are observed. However, they are much more visible in ZTA-LE3 than in ZTA-LE1 (ZTA-LE2 is a middle case). In ZTA-LE1 the bottom of the patterns are pitted. ZTA-LE1 also exhibits the classical microstructure of ZTA material (Figure 8b), with clearly defined zirconia and alumina grains, although the surface is highly rough. In addition to these expected features, small platelets can be seen protruding from the surface.

In ZTA-LE2 the patterns are straight and well defined. In ZTA-LE3 they are a little bit wobbly and large cracks can be seen everywhere in the LE zone. Both ZTA-LE2 and ZTA-LE3 exhibit some “cauliflower” structures on their surface (more probably a packing of intertwined platelets, see Figure 8-f), believed to have been recrystallized from the material evaporated by the laser since they mainly appear on the bottom of the laser tracks. Cracks can also be detected running all along the lased zones in ZTA-LE3.

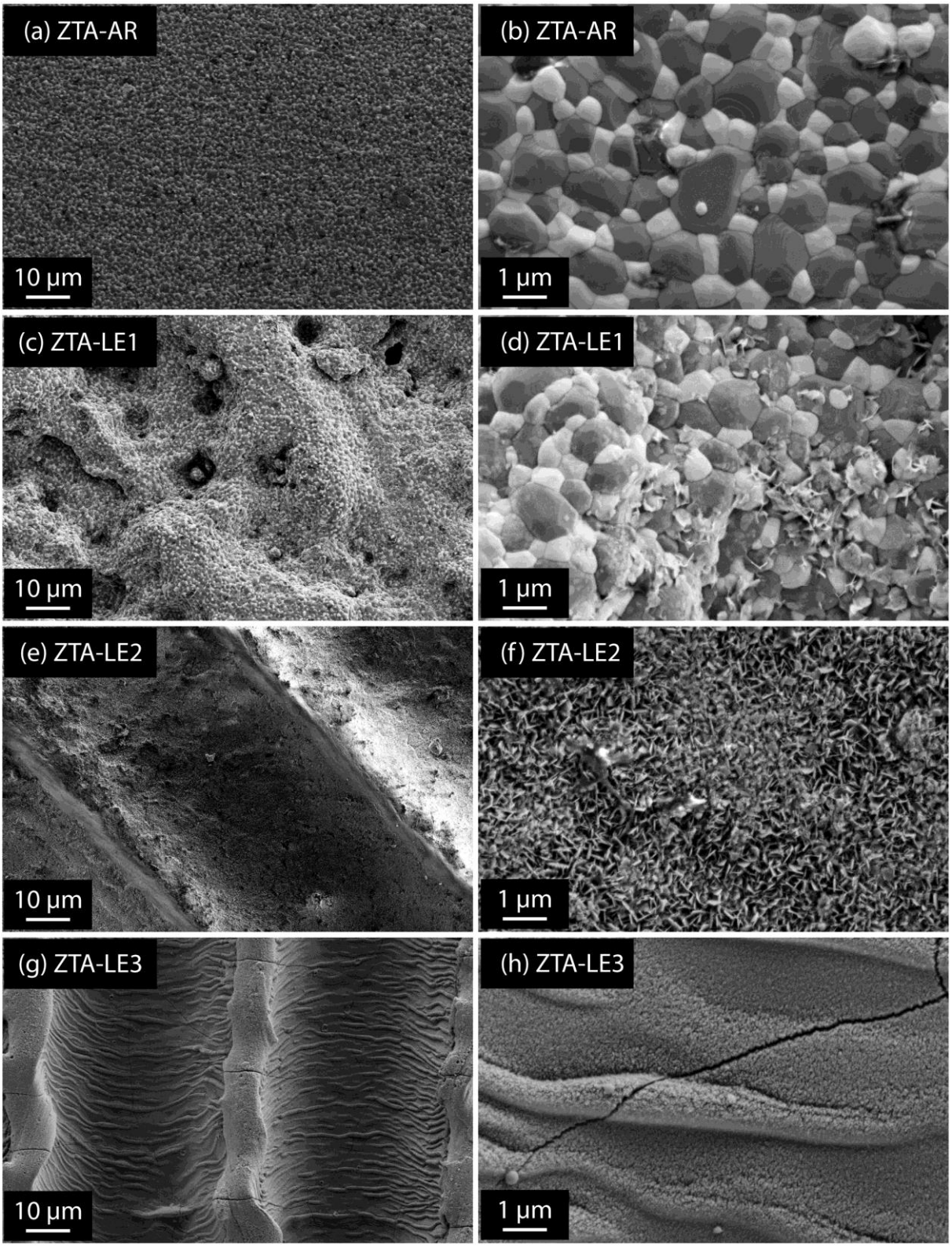

Figure 8: ZTA material, top view by SEM of as-received (AR, a-b) and laser engraved (LE, c-h) zones

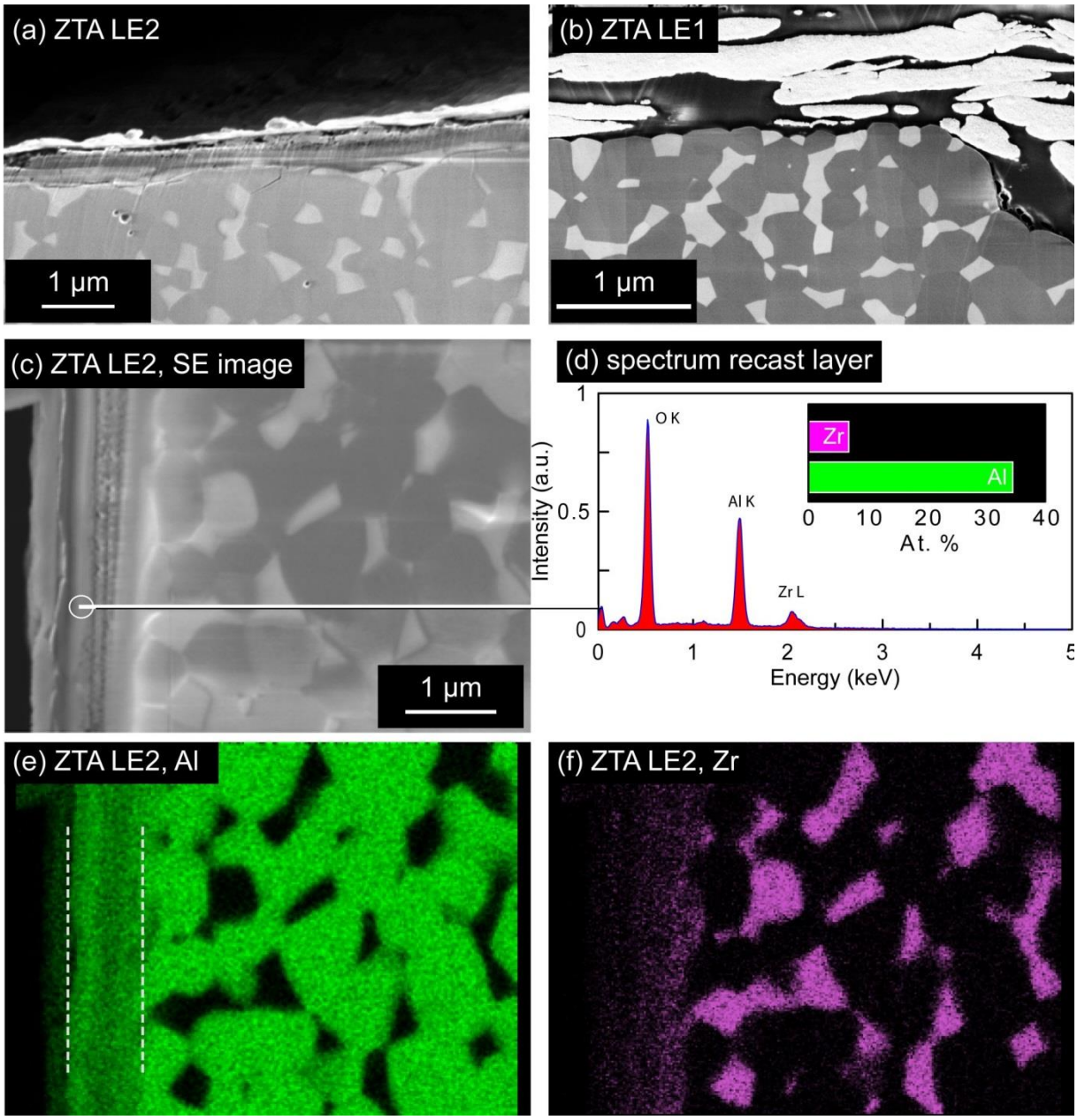

Figure 9: (a) and (b): cross-sectional view of ZTA LE2 and LE1 (SEM); (c)-(f): EDS Map of ZTA LE 2 cross section (in FIB: bottom 4 panels)

The cross-sectional view of ZTA-LE2 shows also the presence of a zirconia-alumina solid solution layer (Figure 9a) with a non-constant alumina/zirconia ratio (it contains around 80 wt.% alumina, similarly to the bulk material). This layer does not exist in ZTA-LE1 material (Figure 9-b). Figure 9-a also shows the presence of small cracks (less than 1 µm deep as seen by SEM).

The 3D-FIB reconstruction shown on Figure 10 confirms the presence of the alumina-zirconia solid solution layer observed before on SEM cross sections. Contrary to ATZ, alumina and zirconia grains seem either completely molten or almost intact: no peripheral molten layer can be clearly distinguished (Figure 10-(c-h)). Much less cracks can be seen under the surface than in ATZ, and they seem discontinuous (Figure 10-b).

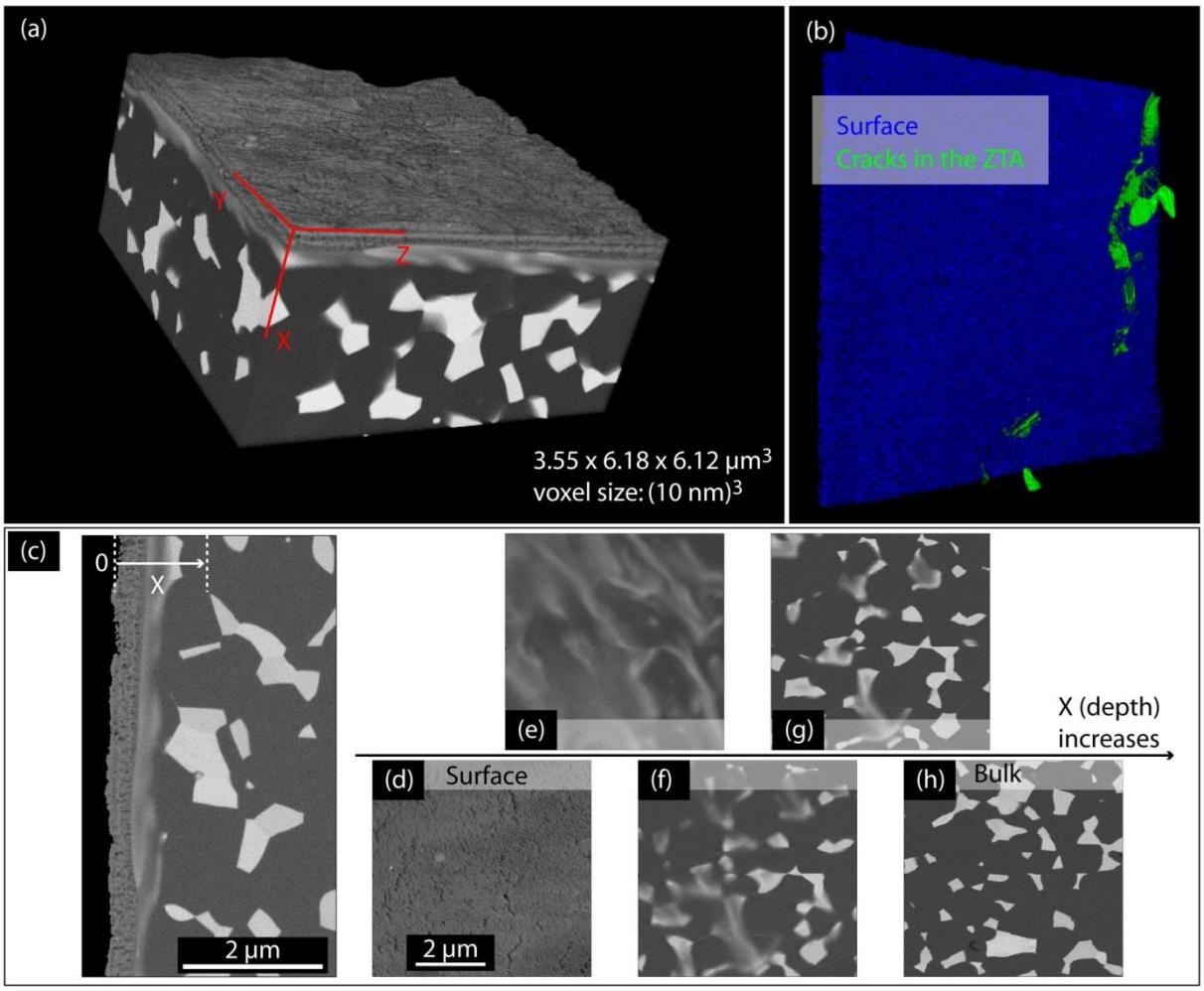

Figure 10: (a) FIB 3D reconstruction of ZTA-LE2 and (b) microcracks network reconstructed from (a). (c): cross section extracted from (a). (d)-(h) sections parallel to the surface (orthogonal to (c)), showing the evolution of the different phases with depth in ZTA LE2; the sections cover the depth indicated by the 2 dashed lines in (c). Zirconia grains appear in white, alumina in grey.

4. DISCUSSION

4.1 INFLUENCE OF LASER ENGRAVING ON HYDROTHERMAL AGEING

To ensure that engraving does not affect the resistance to hydrothermal ageing of implanted hip prostheses heads, it may be of interest to compare the ageing kinetics measured on commercial femoral heads fabricated from the same material and with the same fabrication process (only the final polishing procedure is different) to what was measured on the AR or LE zones. This comparison is shown on Figure 11 for the case of samples treated using lot 2 experimental conditions (these conditions are the most similar to industrial laser engraving conditions). Note that the surface of the discs used here is equivalent to the surfaces of the heads where the laser engravings are suited (not to the polished surface, on which laser engraving cannot be performed, but on which ageing behaviour was assessed).

As shown on Figure 11-a, on ATZ no obvious difference between heads and AR zones can be seen; when conducting the extrapolation at 37°C, the head lies between ATZ-AR and ATZ-LE2 (the two extreme cases).

On ZTA, the results are much more scattered (Figure 11-b). Indeed, at 134°C the heads age faster than AR zones, but at the same rate as LE2. This difference may be due to internal stresses arisen from polishing or laser engraving processes that can accelerate ageing. However the heads seem to age much faster than both AR and LE2 at 37°C. This is probably an artefact due to the very small amount of monoclinic phase created during ageing of ZTA materials, that makes very difficult the measurement of the activation energy, thus makes very unprecise the extrapolation of ageing behaviour at low temperature for both heads, LE and AR conditions.

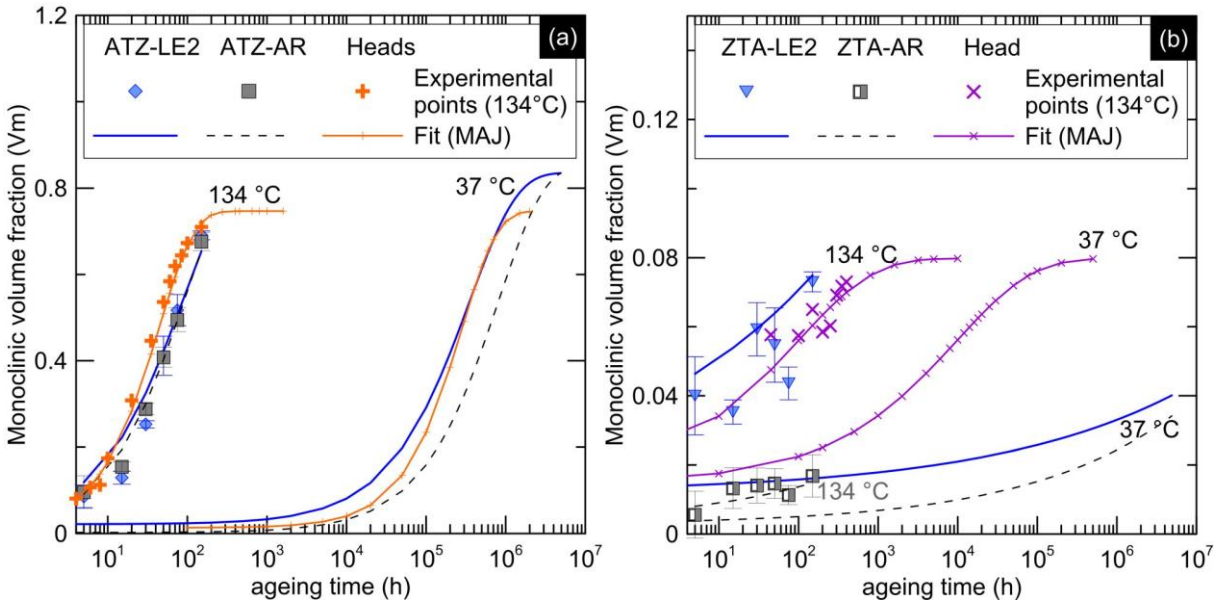

Figure 11: Comparison of ageing kinetics between laser engraved zones and femoral heads. Blue lines and symbols represent the heads, green ones the AR or LE2 areas. (a): ATZ; (b): ZTA.

In all cases, it can be concluded from this stydu that laser engraving with conditions 1 and 2 do not present any risk as far as hydrothermal ageing is concerned**.**

4.2 INFLUENCE OF LASER ENGRAVING ON MICROSTRUCTURES

During the interaction of a laser pulse with a material, several phenomena can usually take place during the laser pulse: heating, formation of a molten pool, ablation (vaporisation can cause an ejection of vapour and molten material) and shock-wave. After the laser pulse, the molten pool cools down to form a recast zone, a layer of surface debris can be formed by both the cooling down of the ejected molten material and the condensation of vaporized material, while microcracks may develop due to the shock wave and to the very localized heating[13]. Such modifications were also observed by Noda et al.[26] on lase zirconia (but with a much higher energy, as can be seen on Fig.1 of [26] showing millimetric pits associated to single, 5 ms pulses, that makes it difficult to compare quantitatively with the process studied here) and by Roitero et al. [27]. Qualitatively the observations performed here (cracking, debris layer, recast layer) are in agreement with the literature. Besides, in ZTA-LE3 wobbly patterns were observed, as if the whole material had been partially molten over a few tenths of micrometres. This is not observed on ATZ-LE3, and may be related to a twice higher energy deposition used on ZTA-LE3 (twice lower scanning speed, see Table 1) and/or to a lower melting point (ZTA being closer to the eutectic composition of the ZrO2 – Al2O3 system (42.5 wt.% ZrO_2 – 57.5 wt.% Al_2O_3)), in spite of better energy dissipation due to the higher thermal conductivity of ZTA as compared to ATZ.

In addition to morphological changes, several authors have also observed a change in composition (loss of oxygen [26,28]) in the lased areas, related to the formation of colour centres [10]. Here the major measurable microstructural change is the formation of a zirconia-alumina solid solution (or at least of a very intimate mixing) with alumina-zirconia proportions close to the overall material in both ATZ and ZTA (lot 2 and 3). Similarly Bartolome *et al.* observed a Al_2O_3-ZrO_2 solid solution containing up to 40 mol.% Al_2O_3 in zirconia-toughened alumina powder obtained by laser co-vaporization of alumina and zirconia [29], and the Al^{3+} ions were found to present a behaviour similar to Y^{3+} ions, substituting the Zr^{4+} ions (and forming many oxygen vacancies). The same phenomena were observed by Zhou *et al.* [30] on a zirconia containing 20 wt.% alumina. These authors also noticed a large displacement of the tetragonal zirconia peak in XRD patterns, attributed to the presence of a large amount of alumina in the zirconia lattice. Such an XRD peak displacement was also observed here: as can be seen in Figure 12-a, the diffraction peaks of ATZ LE2 and LE3 are deformed and/or displaced on their right side. In order to model correctly the experimental XTD diagram (by using Topas® software) the introduction of a second tetragonal phase (labelled "t-ZrO2 sol solution") is necessary (example with ATZ-LE2 sample is shown in Figure 12-b). This is also coherent with the observations of Ackerl et al. [18] on laser-machined ZTA dental implants. The development of these solid solutions is indeed compatible with the formation of a molten pool in which both liquid alumina and zirconia are homogeneously mixed, followed by a rapid cooling (quenching) that prevents the stable state to be reached (at equilibrium, the solubility limit of alumina in zirconia is around 0.3wt.%[31,32] and that of zirconia in alumina is below 0.03 wt.% [32], very low values in comparison with several percent observed here).
Moreover, it is interesting to remark that the thermal treatments involved in the present work never led to the formation of the eutectic structures commonly observed in the literature after fast thermal treatments, whether they involve plasma spraying [30], oxyacetylene flame remelting[33] or laser fusion[34,35] by a continuous laser. This hints to faster treatments than what is usually found in the literature, coherently to us using a pulsed laser.

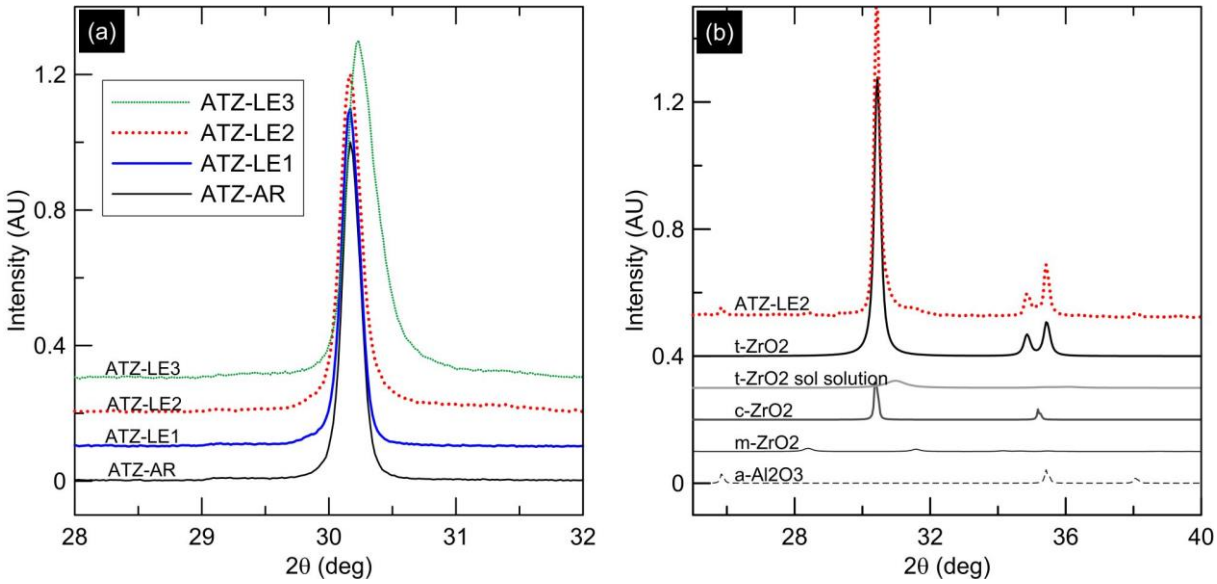

Figure 12: (a) XRD diagrams of the 4 ATZ materials, centred on the most intense tetragonal peak; (b) example of decomposition of a diagram of ATZ-LE2 into 5 phases (using Topas® software): α-alumina, monoclinic, cubic, tetragonal and "tetragonal solid solution" zirconia. The later reflects the contribution of the Al-ZrO solid solution (upper layer) to the diffractogram.

A large difference in the morphologies and topographies obtained with the different laser engraving treatments was observed. The first notable feature is the irregularity of the patterns obtained on LE1 zones, combined with a very homogeneous microstructure. These features can be explained by the fact that lot 1 has been laser engraved in the green state, before sintering. Firstly, this involved the interaction of the laser with a less resistant and homogeneous material, in the sense that during laser engraving lot 1 was not yet sintered thus contained a large amount of porosity, and three phases (pores, alumina and zirconia) that could scatter the laser and blur the laser path. Secondly, diffusion and shrinkage occurred during sintering (thus after laser engraving), allowing the material to develop an equilibrium microstructure consisting of well-defined alumina and zirconia grains. However, one can observe that the return to equilibrium is not complete in ZTA-LE1, since a few remaining flakes can be seen on Figure 8-d).
Both LE2 and LE3 present "flake-like" surface layer (debris) and exhibit a recast layer on top of the bulk material.
Table 4 also indicates that the distance between laser line is smaller in ATZ-LE1 (44 µm *vs* 50 µm for the others, 50 µm being the theoretical hatch distance), which is certainly again due to the shrinkage that occurred in LE1 samples during sintering the process (engraving at 50 µm in the green state, and considering a typical 15% linear shrinkage during sintering, will give a distance of 42.5 µm in the sintered state, compatible with what was observed). For materials ATZ and ZTA the laser parameters 3 are inducing the highest roughness, and the most defined engraving, compared to parameters 1 and 2.

The unusual features characterizing the diffraction peaks of ATZ-LE2 and ATZ-LE3 and shown in Figure 12 might be explained by one or several of the following hypotheses. The enlargement at the right side of the peak's base can be due to any possible distortion of the lattice (due to compressive, residual stresses or to a chemical change, most probably related to the presence of the alumina-zirconia solid solution) or might be a consequence of the roughness of the samples. However, the later hypothesis can be discarded, since the XRD diagrams of ATZ-LE1 do not show this enlargement while the roughness of LE1 and LE2 are quite similar. Thus lattice distortions should be the primary origin the peak widening. The displacement and distortion of the (101) tetragonal peak located neat 30 deg(2θ) can be related to the fact that it's composed of several peaks corresponding to several phases: in addition to the "normal" (101) peak of the tetragonal phase (seen by XRD more than 1 µm below the surface), the (111) peak of the cubic phase is usually found on the left-hand side of the tetragonal peak. Besides, the alumina-zirconia solid solution gives rise to a distorted tetragonal phase as shown by Zhou et al.[30], thus to another peak; the fact that this one is on the right side of the usual (101) tetragonal peak hints to smaller lattice parameters, coherently with the small size of alumina ions as compared to zirconia ions. In addition, the tetragonal peak might contain a peak of tetragonal prime metastable phase (t', not detected here), which usually forms during fast cooling of cubic phase (this may occur since part of the material is molten under the laser beam, thus should go through a cubic state before becoming tetragonal or t').
To find out if these hypotheses are relevant, a precise investigation of the structures involved should be conducted by performing extensive Rietveld refinement analysis and Transmission Eelectron Microscopy diffraction and EELS studies (such an assessment is beyond the scope of this study).

4.3 HYPOTHESES ON THE ORIGIN OF THE COLOUR

Since ATZ-LE1 and ATZ-LE2 have similar roughness but very different colours (dark for LE2, off-white for LE1 like the AR material), the colour is clearly not related to the engraving depth. Moreover, when the laser engraving is performed in the green state (lot 1) then the markings

are also coloured, but much less intense than in the sintered state (only visible in ATZ) and the colour vanishes during sintering process. This shows that the laser treatment always induces the colour change but that the colour vanishes with heat treatment.
Several explanations of this colour have been proposed in the literature: mainly, induction of colour centres by the laser beam [10], formation of additional oxygen vacancies [11] or formation of zirconium carbide [9] or nitride [6,8] (using atmosphere or contamination layer as carbon or nitrogen sources). Unfortunately the results obtained here are coherent with all these hypotheses; hence none can be discarded for now.
To get more inside in the origin of the colour, a more detailed microstructural analysis should be performed. It would include TEM to characterize more in details the recast layer (is it homogenous, or a very fine dispersion of alumina and zirconia grains not observable by SEM?), and X-ray Photoelectron Spectroscopy (XPS) analysis to observe the potential formation of oxygen vacancies and colour centres.

5. CONCLUSIONS

Zirconia toughened alumina (ZTA) and alumina toughened zirconia (ATZ) materials used for orthopaedic applications were submitted to laser engraving. The specific purpose of this paper was to assess how the surface and sub-surface modifications brought by the laser could influence (positively or negatively) the durability of the ceramic components, and in particular their hydrothermal ageing resistance.
The experiments performed here proved that hydrothermal ageing was not much affected by laser treatment. Especially in comparison with total hip replacement heads made from the same materials, ageing of the Laser Engraved zones is either slower or comparable.
Besides, the heat affected zone was very thin (around a micron at most), almost no cracks (and very small) were found in ZTA and the crack network observed in ATZ materials subjected to the most severe lasing condition did not extend into the bulk (it is limited to ~2 µm depth). Hence the defects induced by laser engraving are not critical, and it is very likely that the laser engraving treatments will cause no decrease in the mechanical resistance of the components, especially if the engravings are positioned on non-loaded zones.
Finally, modification of the chemistry of the sub-surface was detected after laser engraving. A re-deposited debris layer containing oxygen, carbon, zirconium and aluminium was observed on the outermost surfaces, on top of a recast alumina-zirconia solid solution. The thickness of these two layers combined was of the order of magnitude of a half micron. The formation of this microstructure is explained by localized melting of the material and very fast cooling rate that quench the microstructure.

Acknowledgments
We acknowledge the CLYM (Centre Lyonnais de Microscopie), supported by the CNRS, the "Grand Lyon" and the Rhône-Alpes Region for the access to the FIB/SEM device used in this study.

6. REFERENCES

[1] A. Stanciuc, Q. Flamant, C. Martin, M. Alini, M. Anglada, M. Peroglio, Femtosecond laser multi-patterning of zirconia for screening of cell-surface interactions, J. Eur. Ceram. Soc. 38 (2018) 939–948. doi:10.1016/j.jeurceramsoc.2017.08.019.

[2] H. Zhou, C. Li, Z. Zhou, R. Cao, Y. Chen, S. Zhang, G. Wang, S. Xiao, Z. Li, P. Xiao, Femtosecond laser-induced periodic surface microstructure on dental zirconia ceramic, Mater. Lett. 229 (2018) 74–77. doi:10.1016/j.matlet.2018.06.059.

[3] R.A. Delgado-Ruíz, J.L. Calvo-Guirado, P. Moreno, J. Guardia, G. Gomez-Moreno, J.E. Mate-Sánchez, P. Ramirez-Fernández, F. Chiva, Femtosecond laser microstructuring of zirconia dental implants, J. Biomed. Mater. Res. Part B. 96 (2011) 91–100. doi:10.1002/jbm.b.31743.

[4] D. Liu, J.P. Matinlinna, J.K. Tsoi, E.H.N. Pow, T. Miyazaki, Y. Shibata, C. Kan, A new modified laser pretreatment for porcelain zirconia bonding, Dent. Mater. 29 (2013) 559–565. doi:10.1016/j.dental.2013.03.002.

[5] B. Henriques, D. Fabris, J.C.M. Souza, F.S. Silva, Ó. Carvalho, M.C. Fredel, J. Mesquita-guimarães, Bond strength enhancement of zirconia-porcelain interfaces via Nd : YAG laser surface structuring, J. Mech. Behav. Biomed. Mater. 81 (2018) 161–167. doi:10.1016/j.jmbbm.2018.02.031.

[6] B.S. Yilbas, Laser treatment of zirconia surface for improved surface hydrophobicity, J. Alloys Compd. 625 (2015) 208–215. doi:10.1016/j.jallcom.2014.11.069.

[7] J. Ihlemann, A. Scholl, H. Schmidt, B. Wolff-Rottke, Nanosecond and femtosecond excimer-laser ablation of oxide ceramics, Appl. Phys. A. 60 (1995) 411–417.

[8] B. Qian, Z. Shen, Laser sintering of ceramics, J. Asian Ceram. Soc. 1 (2013) 315–321. doi:10.1016/j.jascer.2013.08.004.

[9] P.P. Shukla, J. Lawrence, Characterization and compositional study of a ZrO2 engineering ceramic irradiated with a fibre laser beam, Opt. Laser Technol. 43 (2011) 1292–1300. doi:10.1016/j.optlastec.2011.03.026.

[10] N. Mansour, K. Mansour, E.W. Van Stryland, M.J. Soileau, Diffusion of color centers generated by two-photon absorption at 523 nm in cubic zirconia, J. Appl. Phys. 67 (1990) 1475–1477.

[11] E. Hontzopoulos, E. Damigos, Excimer Laser Surface Treatment of Bulk Ceramics, Appl. Phys. A. 52 (1991) 421–424.

[12] J. Chevalier, L. Gremillard, S. Deville, Low-Temperature Degradation of Zirconia and Implications for Biomedical Implants, Annu. Rev. Mater. Res. 37 (2007) 1–32. doi:10.1146/annurev.matsci.37.052506.084250.

[13] J. Peter, B. Doloi, Bhattacharyya, Nd:YAG Maser Marking on Zirconia Ceramics, Laser Based Manuf. (2015) 283–316. doi:https://doi.org/10.1007/978-81-322-2352-8_16.

[14] E. Roitero, F. Lasserre, J.J. Roa, M. Anglada, F. Mücklich, E. Jiménez-Piqué, Nanosecond-laser patterning of 3Y-TZP: Damage and microstructural changes, J. Eur. Ceram. Soc. 37 (2017) 4876–4887. doi:10.1016/j.jeurceramsoc.2017.05.052.

[15] C. Wei, L. Gremillard, The influence of stresses on ageing kinetics of 3Y- and 4Y-stabilized zirconia, J. Eur. Ceram. Soc. 38 (2018) 753–760. doi:10.1016/j.jeurceramsoc.2017.09.044.

[16] E. Roitero, M. Ochoa, M. Anglada, F. Mücklich, E. Jiménez-Piqué, Low temperature degradation of laser patterned 3Y-TZP: Enhancement of resistance after thermal treatment, J. Eur. Ceram. Soc. 38 (2018) 1742–1749. doi:10.1016/j.jeurceramsoc.2017.10.044.

[17] E. Roitero, M. Anglada, F. Mücklich, E. Jiménez-Piqué, Mechanical reliability of dental grade zirconia after laser patterning, J. Mech. Behav. Biomed. Mater. 86 (2018) 257–

263. doi:10.1016/j.jmbbm.2018.06.039.
[18] N. Ackerl, M. Warhanek, J. Gysel, K. Wegener, Ultrashort-pulsed laser machining of dental ceramic implants, J. Eur. Ceram. Soc. 39 (2019) 1635–1641. doi:10.1016/j.jeurceramsoc.2018.11.007.
[19] S. Fiedler, R. Irsig, J. Tiggesbäumker, C. Schuster, C. Merschjann, N. Rothe, S. Lochbrunner, M. Vehse, H. Seitz, E.D. Klinkenberg, K.H. Meiwes-Broer, Machining of biocompatible ceramics with femtosecond laser pulses, Biomed. Eng. Biomed. Tech. 58 (2013) 19–20. doi:10.1515/bmt-2013-40.
[20] A. Carvalho, L. Cangueiro, V. Oliveira, R. Vilar, M.H. Fernandes, F.J. Monteiro, Femtosecond laser microstructured Alumina toughened Zirconia: A new strategy to improve osteogenic differentiation of hMSCs, Appl. Surf. Sci. 435 (2018) 1237–1245. doi:10.1016/j.apsusc.2017.11.206.
[21] L. Goyos-Ball, C. Prado, R. Díaz, E. Fernández, A. Ismailov, T. Kumpulainen, E. Levänen, R. Torrecillas, A. Fernández, The effects of laser patterning 10CeTZP-Al2O 3 nanocomposite disc surfaces: Osseous differentiation and cellular arrangement in vitro, Ceram. Int. 44 (2018) 9472–9478. doi:10.1016/j.ceramint.2018.02.164.
[22] M. Aivazi, M. hossein Fathi, F. Nejatidanesh, V. Mortazavi, B. HashemiBeni, J.P. Matinlinna, O. Savabi, The evaluation of prepared microgroove pattern by femtosecond laser on alumina-zirconia nano-composite for endosseous dental implant application, Lasers Med. Sci. 31 (2016) 1837–1843. doi:10.1007/s10103-016-2059-8.
[23] L. Gremillard, C. Wei, J. Chevalier, K. Hans, T. Oberbach, A fast, stepwise procedure to assess time-temperature equivalence for hydrothermal ageing of zirconia-based materials, J. Eur. Ceram. Soc. 38 (2018) 181–186. doi:10.1016/j.jeurceramsoc.2017.08.018.
[24] R.C. Garvie, P.S. Nicholson, Phases analysis in zirconia systems, J. Am. Ceram. Soc. 55 (1972) 303–305.
[25] H. Toraya, M. Yoshimura, S. Somiya, Calibration curves for the quantitative analysis of the monoclinic-tetragonal ZrO2 system by X-ray diffraction, J. Am. Ceram. Soc. 67 (1984) C119–C121.
[26] M.N. Noda, U. Okuda, J. Tsuruki, Y. Minesaki, Y. Takenouchi, S. Ban, Surface damages of zirconia by Nd:YAG dental laser irradiation, Dent. Mater. J. 29 (2010) 536–541. doi:10.4012/dmj.2009-127.
[27] E. Roitero, F. Lasserre, M. Anglada, F. Mücklich, A parametric study of laser interference surface patterning of dental zirconia : Effects of laser parameters on topography and surface quality, Dent. Mater. 33 (2016) e28–e38. doi:10.1016/j.dental.2016.09.040.
[28] D.K. Chatterjee, S.K. Ghosh, D.M. Korn, Method of controlled laser imaging of zirconia alloy ceramic lithographic member to provide localized melting in exposed areas, 5839369, 1998.
[29] J.F. Bartolomé, A. Smirnov, H. Kurland, J. Grabow, F.A. Müller, New ZrO2 / Al2O 3 Nanocomposite Fabricated from Hybrid Nanoparticles Prepared by CO2 Laser Co-Vaporization, Sci. Rep. 6:20589 (2016) 1–11. doi:10.1038/srep20589.
[30] X. Zhou, V. Shukla, W.R. Cannon, B.H. Kear, Metastable Phase Formation in Plasma-Sprayed ZrO2 (Y2O3)– Al2O3, J. Am. Ceram. Soc. 86 (2003) 1415–1420.
[31] S. Tekeli, The solid solubility limit of Al2O3 and its effect on densification and microstructural evolution in cubic-zirconia used as an electrolyte for solid oxide fuel cell, Mater. Des. 28 (2007) 713–716. doi:10.1016/j.matdes.2005.09.011.
[32] M.A.J. Stough, J.R. Hellmann, Solid Solubility and Precipitation in a Single-Crystal Alumina – Zirconia System, J. Am. Ceram. Soc. 85 (2002) 2895–2902.
[33] Z. Wang, J. Ouyang, Y. Wang, Z. Liu, Y. Ma, L. Xie, Nucleation and epitaxial growth

of highly textured Al2O3 – ZrO2 nanoeutectic rapidly solidified from oxyacetylene flame remelting, Ceram. Int. 44 (2018) 22027–22031. doi:10.1016/j.ceramint.2018.08.204.
[34] Z. Wang, J. Ouyang, Y. Wang, L. Xie, Y. Ma, Z. Liu, A. Henniche, Y. Wang, Microstructural characterization of nanostructured Al2O3 -ZrO2 eutectic layer by laser rapid solidification method, Appl. Surf. Sci. 476 (2019) 335–341. doi:10.1016/j.apsusc.2019.01.096.
[35] F.J. Ester, A. Larrea, R.I. Merino, Processing and microstructural study of surface laser remelted Al2 O3 – YSZ – YAG eutectic plates, J. Eur. Ceram. Soc. 31 (2011) 1257–1268. doi:10.1016/j.jeurceramsoc.2010.08.016.